

RSC Advances



This is an *Accepted Manuscript*, which has been through the Royal Society of Chemistry peer review process and has been accepted for publication.

Accepted Manuscripts are published online shortly after acceptance, before technical editing, formatting and proof reading. Using this free service, authors can make their results available to the community, in citable form, before we publish the edited article. This *Accepted Manuscript* will be replaced by the edited, formatted and paginated article as soon as this is available.

You can find more information about *Accepted Manuscripts* in the [Information for Authors](#).

Please note that technical editing may introduce minor changes to the text and/or graphics, which may alter content. The journal's standard [Terms & Conditions](#) and the [Ethical guidelines](#) still apply. In no event shall the Royal Society of Chemistry be held responsible for any errors or omissions in this *Accepted Manuscript* or any consequences arising from the use of any information it contains.



Journal Name

ARTICLE

Tailoring the optical properties of ZnO nano-layers and their effect on *in-vitro* biocompatibility

Vincent Rogé,^{a,b} Anastasia Georgantzopoulou,^c Kahina Mehennaoui,^c Ioana Fecheté,^b François Garin,^b Aziz Dinia,^d Arno C. Gutleb,^c and Damien Lenoble^{*a}

Received 00th January 20xx,
Accepted 00th January 20xx

DOI: 10.1039/x0xx00000x

www.rsc.org/

This paper highlights the use of Al₂O₃ and SnO₂ films as protecting layers to tailor the optical properties and biocompatibility of ZnO nano-films. ZnO, ZnO/Al₂O₃ and ZnO/SnO₂ nano-films have been deposited inside 3-dimensional (3D) structures such as anodic aluminium oxide (AAO) membranes via a gas phase atomic layer deposition (ALD) process. We show that ZnO/Al₂O₃ multilayers exhibit improved excitonic photoluminescence properties compared to ZnO only, whereas ZnO/SnO₂ multilayers quench the near band edge emission signal. In addition, *in-vitro* experiences on Caco-2/TC7 cells and *Vibrio fischeri* bacteria reveal that ZnO/Al₂O₃ and ZnO/SnO₂ multilayers display an enhanced biocompatibility in liquid media compared to ZnO. We attribute the improvement of the biocompatibility to a lower dissolution of the ZnO nano-film when protected by Al₂O₃ or SnO₂.

Introduction

Zinc oxide is a semiconductor material of high interest for applications in several different fields. Due to its direct band gap of approximately 3.2 eV, its exciton binding energy of 60 meV and its near ultraviolet emission¹, it is a potential material for optical and electronic devices such as UV laser diodes, photodetectors and piezoelectric nano-generators². It is also used as a photocatalytic material for the degradation of organic pollutants³ and in solar cells^{4,5}. The synthesis of one-dimensional (1D) ZnO nano-structures such as nano-wires or nano-rods to tailor its properties is of grand interest, especially with regard to tuning its optical response and surface-to-volume ratio⁶. Porous anodic alumina membranes are widely used templates for the synthesis of 1D ZnO materials, due to their high pore aspect ratio and their chemical and thermal stability. It allows the development of ordered nano-wires inside pores⁷, can serve as a template for the growth of conformal nano-films with a large specific area⁸, and is of interest for the development of next generation nano-devices in optoelectronics, sensors, or information storage⁹.

The development of heterostructures based on ZnO is another approach to modulate ZnO optical and opto-chemical

properties. ZnO/polymer, ZnO/Er₂O₃ and ZnO/ZnMgO core/shell structures have been previously studied for the improvement of the UV photoemission¹⁰. For example, Richters et al. have shown that a surrounding layer of Al₂O₃ around ZnO nano-wires can increase the UV optical luminescence¹¹. Other such examples are ZnO/SnO₂, TiO₂/SnO₂, ZnO/WO₃ or SnO₂/ZnO¹² heterostructures, which have been studied for the improvement of the separation and increased lifetime of photo-generated holes h⁺ and electrons e⁻ carriers, due to the formation of a heterojunction between the two materials. This effect has been shown to promote their photocatalytic activity. Al₂O₃ and SnO₂ are materials with a higher band gap than ZnO (6.4 eV and 3.8 eV, respectively). They are therefore transparent to UV-A light, while ZnO absorbs in this range. This makes Al₂O₃ and SnO₂ attractive materials for the development of heterostructures to be used in optical and opto-chemical devices based on ZnO.

With the increasing human exposure to such nanostructures¹³, it is essential to evaluate the toxicological risks associated with their development and use. Various studies have focused on the *in-vitro* biocompatibility of ZnO, with most of them concerned only with the state of the nano-particles. It is known that nano-particles are highly active due to their size and surface state, even if they are composed of inert materials^{14,15}. Previous studies have shown that at the nanoscale, ZnO particles can exhibit oxidative, genotoxic, and cytotoxic effects^{16,17,18}. Understanding the origin and the mechanism involved in these toxicological processes is critical for advancing toward safer materials. Poynton et al. suggested that ZnO nano-particles themselves, as well as the Zn²⁺ ions resulting from their dissolution, can be toxic, but that the mechanism involved in these two cases is different¹⁹. The synthesis of ZnO materials on a template appears a suitable

^a Material Research and Technology (MRT) Department, Luxembourg Institute of Science and Technology (LIST), 5, avenue des Hauts-Fourneaux, L-4362 Esch-sur-Alzette Luxembourg, e-mail: damien.lenoble@list.lu

^b Institut de Chimie et Procédés pour l'Energie, l'Environnement et la Santé (ICPEES), UMR 7515, 25 rue Becquerel, 67087 Strasbourg cedex 2, France, email: garin@unistra.fr

^c Environnemental Research and Innovation (ERIN) Department, Luxembourg Institute of Science and Technology (LIST), 5, avenue des Hauts-Fourneaux, L-4362 Esch-sur-Alzette Luxembourg, e-mail: arno.gutleb@list.lu

^d Institut de Physique et Chimie des Matériaux de Strasbourg (IPCMS), UMR 7504, 23 rue du Loess, 67034 Strasbourg cedex 2, France, e-mail: aziz.dinia@ipcms.unistra.fr

technique for preventing the particle toxicity effect by fixing it to avoid a direct contact with living systems. The dissolution of those fixed particles in aqueous systems is still a limiting problem. Thus, we aim at developing a system that tunes the optical properties of ZnO materials while preventing their negative environmental impact. To this end, heterostructures of ZnO/Al₂O₃ and ZnO/SnO₂ have been synthesised via a gas phase atomic layer deposition (ALD) technique inside porous anodic aluminium oxide (AAO). ALD has been used for its ability to grow homogeneous and conformal metal-carbide films, metal oxide films or metallic films, even on complex 3D structures²⁰. Our strategy is to protect the potentially soluble ZnO with insoluble materials like Al₂O₃ or SnO₂, without impairing the targeted ZnO optical properties. Nano-particles of Al₂O₃ have been shown to be toxic to *C. elegans* nematode, especially to its reproductive capability^{21,22}, while the toxicity of continuous coatings of Al₂O₃ nano-films are still under investigation. One shall note that plain materials of Al₂O₃ are used in commercial water treatment technologies²³. Considering that Al₂O₃ and SnO₂ materials are almost insoluble in water and that their ALD coatings are mechanically stable on the sample (no delamination of the nano-films), the toxicity of these films shall be strongly prevented while they screen the toxicity of the ZnO under-layers...

The effects of the membranes in the absence of direct contact were evaluated with the use of an *in vitro* intestinal cell culture model (Caco-2/TC7) and the standard ecotoxicological bioassay using the marine bacteria *Vibrio fischeri* as a model organism. Caco-2/TC7 cells have been chosen as target cells in order to determine if a possible harmful behaviour of ZnO-based materials could appear when used in water, especially concerning ZnO-based photocatalytic materials such as ZnO and ZnO/SnO₂. Indeed, an instability of the material in water could lead to its dissolution or delamination, and thus to an exposure to human beings when the said-water is drunk.

The objective of this work is to study heterostructures of ZnO/Al₂O₃ and ZnO/SnO₂ to identify the most suitable strategy for the safe use of ZnO-based photocatalytic devices in aqueous environments.

EXPERIMENTAL SECTION

Experimental processes

All of the chemicals employed in this study were purchased from Sigma-Aldrich and used as received. Commercial AAO membranes from Anapore, with an average pore diameter of 200 nm and thickness of 150 μm, were used. High purity grade (100) single side polished silicon wafers were obtained from Siegert Wafer. Flat silicon wafers were used as a substrate for some physico-chemical characterisations of our system. Zinc oxide (ZnO), alumina (Al₂O₃) and tin oxide (SnO₂) films were grown using a gas phase ALD process in a TF200 ALD instrument (Beneq, Finland). For the development of ZnO, diethyl zinc (DEZ) (99.99 %) was chosen as a zinc precursor and distilled water was used as an oxidant. They were kept in canisters under vacuum at room temperature and injected

into the reacting chamber without any carrier gas. Reaction was achieved at low pressure (0.5-5 mBar) using nitrogen as a carrier gas. The ALD cycles were as follows: DEZ injection pulse – purge – water injection pulse – purge. The pulse lengths were chosen to be between 100-300 ms, and the purges 2 s to achieve homogenous growth inside the porous structures. The temperature of the reactor was maintained at 200 °C. The number of cycles was adjusted to produce a 20 nm thick film with a growth rate of approximately 5 Å per cycle.

The Al₂O₃ ALD deposition was performed using trimethylaluminium (TMA) (99.99 %) as the aluminium source and distilled water as the oxidant. The injection conditions used were the same as those previously described for ZnO. The growth temperature inside the reaction chamber was maintained at 200 °C and the number of cycles was adjusted to achieve a 20 nm homogeneous film as well, with a growth rate of approximately 1 Å per cycle. SnO₂ films were grown with tin chloride (SnCl₄) (99.99 %) as the tin source and distilled water as the oxidant. The injection conditions were the same as those previously described for the ZnO and Al₂O₃ films. The reaction was carried out at approximately 300 °C using a number of cycles that allowed for the growth of a 60 nm rough film; the growth rate was approximately 0.3 Å per cycle.

Characterisation technics

The morphology of the nano-films was investigated by scanning electron microscopy (SEM) using a high resolution Helios 50 microscope (FEI, USA) at an acceleration voltage of 2 kV to avoid charging of the isolating AAO substrate. SEM images were also used to estimate the size of the grain seen on the surface. Optical properties of the developed structures were studied by photoluminescence with an Infinite M1000 pro UV-visible spectrometer (TECAN, Switzerland). The analyses were performed under light irradiation at a 280 nm wavelength, with scanning detection carried out from 300 nm to 700 nm. The crystallographic structure of the films was investigated by X-ray diffraction (XRD) using a D8 Discover diffractometer (Bruker, USA) with a Cu K α X-ray source ($\lambda=0,1542$ nm). The chemical composition and stoichiometry was characterised by X-ray photoelectron spectroscopy (XPS) with an Axis Ultra DLD X-ray spectrometer (Kratos Analytical Ltd, UK) equipped with a monochromatic Al K α x-ray source ($\lambda=0,8343$ nm) operated at 150 W. The contact potential difference of the surfaces was evaluated by kelvin probe force microscopy (KPFM). KPFM measurements were performed in a dry atmosphere (<10 % humidity maintained for 2 hours prior to starting the measurement) on a Multiview 4000 atomic force microscope (Nanonics, Israel) using single path mode. Both the topography and the KPFM images were recorded simultaneously, the latter using a.c. excitation at a high-frequency harmonic resonance of the cantilever. An ACCESS-FM Si tip (AppNano, USA) with a resonance frequency of 70 kHz was employed, and the KPFM signal was recorded at the harmonic resonance of 434 kHz. To verify the repeatability of the measurement, we performed measurements on the different samples successively and observed a change of less

than 10 mV for measurements repeated on the same sample. The total zinc, tin and aluminium content in the cell culture solutions was measured using inductively coupled plasma mass spectrometry (ICP-MS) with a Elan DRC-e spectrometer (Perkin Elmer, USA).

In vitro cytotoxicity evaluation

The human colon cancer Caco-2 cell line sub-clone TC7 (Caco-2/TC7) was received as a generous gift from Monique Rousset (Paris, France). Phosphate buffered saline (PBS) and heat-inactivated fetal bovine serum (FBS) were both obtained from Invitrogen (Merelbeke, Belgium).

The cells were maintained in Dulbecco's Modified Eagle Medium-Glutamax (DMEM-Glutamax, Invitrogen) supplemented with 10 % fetal bovine serum, 1 % non-essential amino acids and 1 % penicillin/streptomycin solution (37 °C, 10 % CO₂ humidified incubator). The medium was renewed every other day and the cells were split upon confluency with Trypsin-EDTA.

The Caco-2/TC7 cells were seeded in 12-well plates at a concentration of 1.2x10⁵ cells/ml (1.5 mL/well, 5x10⁴ cells/cm²) and cultured for 14 days at 37 °C in a 10 % CO₂ humidified incubator. The medium was renewed every other day.

Sample preparation: The samples provided for testing were 13 mm diameter AAO, which corresponds to a specific area of approximately 217 cm². Prior to exposure the samples were sterilized in ethanol for 10 minutes and then washed twice with cell culture medium.

Exposure: After 14 days, the medium was discarded and 1.5 mL of new medium was added in each well. The samples were placed in 12-well polycarbonate 0.4 μM pore size Transwell inserts containing 1 ml cell culture medium to prevent direct contact of the cells with the AAO (Figure 1) and were incubated for 24 hours at 37 °C in a 10 % CO₂ humidified incubator.

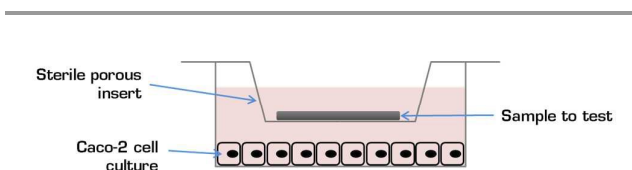


Figure 1 Experimental setup for assessing the cytotoxicity of the samples in the absence of direct contact with the cells.

Metabolic activity assay

At the end of the exposure period the Transwell inserts containing the samples were removed and the supernatant was kept for ICP-MS analysis to determine the Zn²⁺ concentration in the solution. Cytotoxicity was determined based on the metabolic activity assay using MTS [3-(4,5-dimethylthiazol-2-yl)-5-(3-carboxymethoxyphenyl)-2-(4-sulfophenyl)-2H tetrazolium salt] as a probe (Promega). 1.3 ml of MTS reagent was added in each well. After 1 hour of incubation the absorbance at 490 nm was measured (Synergy

2, BioTek Instruments, Inc.). The reported metabolic activity is expressed relative to the untreated group, which was set at 100 %.

Vibrio fischeri inhibition of luminescence assay

Porous membranes with ZnO, ZnO/Al₂O₃ and ZnO/SnO₂ films were separately placed in petri dishes. 15 ml of Volvic water (France) was added, and the samples were immersed for 48 h at 18 °C in the dark. 1 ml of each sample was then taken for the *V. fischeri* test. The rest (remaining water) was stored at 4 °C until performing the ICP-MS analysis.

Vibrio fischeri exposure

The marine bioluminescent bacteria *V. fischeri* is a broadly used organism for screening the toxicity of chemicals, environmental samples and nanoparticles^{24,25,26}. The assay used was adapted from the ISO standard (International Organisation for Standardisation, ISO 11348-1, 1999) for use in a 96-well plate, as previously described (Georgantzopoulou et al. 2013). *V. fischeri* bacteria (DSMZ, Germany) in a 10 % glycerol solution were stored at -80 °C. After thawing, an activation solution was added to the bacterial stock, which was then further diluted in a 2 % NaCl solution. 50 μl portions of this bacterial suspension were introduced in each well of the 96-well plate. The water solution taken after incubation with the porous membranes was serially diluted in a 2 % NaCl solution and 100 μl of each solution was introduced in the wells. The 2 % NaCl diluent was used as a control. After 30 min of exposure, the luminescence activity was measured using a Synergy 2 luminometer (BioTek Instrument, Inc, USA). Three replicate measurements were performed for each treatment and control sample.

Statistical analysis

All of the results are reported as the mean ± SD of three independent experiments each performed in triplicate. The viability rates in the tested conditions were compared and significant heterogeneity among the tested conditions ($P < 0.05$) was observed. Therefore, a non-parametric Kruskal-Wallis test for multiple independent groups followed by a Mann-Whitney U-test was performed. All of the statistical analyses were carried out using the Statistica 7.0 software package (Statsoft Inc).

RESULTS AND DISCUSSION

Physico-chemical characterisations

Cross-sectional SEM images were recorded to visualise the different films grown inside the porous AAO structures. A 20 nm ZnO nanofilm can be clearly observed in Figure 2b, which reveals that it is a polycrystalline film with a grain size of approximately 13-20 nm. The image also provides evidence of the conformality of the deposition. The cross-sectional image shown in Figure 2c reveals a homogeneous smooth Al₂O₃ layer deposited on top and entirely covering the zinc oxide. Deposition of the SnO₂ was verified from the image shown in

Figure 2d. The morphology of the SnO_2 grown in AAO differs from that of the ZnO or Al_2O_3 films. The former exhibits tetragonal grains rather than the conformal films produced by the latter two. This is, to the best of our knowledge, the first time that such structures have been observed for a SnO_2 ALD synthesis inside AAO. The morphology is attributed to the use of a chlorinated precursor, SnCl_4 . It has been previously assumed²⁷, for the growth of TiO_2 , that because of the adsorption of chlorine, originating from the chlorinated precursor TiCl_4 , at the surface of the growing TiO_2 , a passivation of the (011) and (100) crystallographic planes of the tetragonal rutile structure could occur; whereas the (002) plan remains active for the growth. As a consequence, nano-rod-like TiO_2 structures are observed. This passivation mechanism is explained by the number of far titanium or near titanium neighbours present at the surface of the different crystallographic planes. A high number of near titanium neighbours statistically promotes the passivation of the surface due to the formation of Ti-O-Ti bonding. Jian Shi *et al.*^{28,29} determined that for the tetragonal structure, (011) and (100) planes have three near titanium neighbours; whereas the (002) plane has only one. For this reason, the (011) and (100) planes are preferentially passivated as compared to the (002) plane, the growth of nano-rods is therefore promoted^{28,29}.

In our case, the growth of SnO_2 seems to be different from what Jian Shi *et al.* observed for TiO_2 . The SnO_2 crystal structure is tetragonal rutile like for TiO_2 , but here tetragonal grains clearly appear in the porous membrane. We do not observe any preferential direction growth that could lead to the formation of nano-rods, revealing a surface passivation. Instead, we attribute the SnO_2 grains morphology to the aggressiveness nature of the HCl by-product released during the ALD growth reaction. During the SnO_2 ALD process, HCl is released from the reaction between SnCl_4 and H_2O (Figure 4). Inside the AAO channels, HCl has a longer residence time into the pores, with multiple interactions with the inner pores surface when compared to a planar surface. As a result, the presence of HCl can lead to the dissolution of the growing structure between two ALD cycles (SnCl_4 and H_2O exposure). A competition appears in the channel of the AAO between the SnO_2 crystallisation and growth and its dissolution/etching induced by HCl by-products. The consequence is the growth of grains instead of conformal films. The Figure 3 depicts the difference in the morphology of SnO_2 grown at the surface of the AAO and inside pores during an ALD process. The presence of a conformal film on the top of the AAO and grains inside pore channels is a giveaway of a change in the growth mechanism of SnO_2 induced by the nano-texturation of the different pores acting like nano-reactors. The corrosive effect of chlorinated compounds and their etching effect on growing structures have already observed in the literature^{30,31}. It is worth mentioning that with the same growth parameters, the synthesis of SnO_2 on a flat surface (like silicon wafers) leads to a homogeneous 60 nm thick rough film, like observed on top of the AAO. This further confirms that the growth of SnO_2 grains in not intrinsically due to the ALD growth mechanisms

but to a competition between films growth and etching by the chlorinated species. For planar surfaces, the colliding events between HCl by-products and the SnO_2 surface is reduced in our process conditions.

The chemical composition of the films was investigated by XPS with an analysis depth of approximately 10 nm. Table 1 shows the relative percentage of each element for all of the processes, from which the presence of a ZnO film with a 1-1 stoichiometry ratio (51-49 %, respectively) of zinc and oxygen can be confirmed. No signal due to the substrate was observed in the SEM images, which reveals a perfect conformality of the ZnO growth process. Regarding the Al_2O_3 deposition, we have verified that the film grown on top of the zinc oxide exhibits a 35-60 % ratio of Al and O. In this case, the conformality of the deposition is again verified by the absence of Zn (1 % of zinc is detected, which is inside the error range of the XPS analysis). The SnO_2 deposition inside AAO is verified by the presence of a 32-60 % ratio of tin and oxygen, respectively. The 4 % of zinc observed in the material corresponds to the underlying ZnO layer, which is visible due to the growth of SnO_2 as particles separated grains than as a conformal film.

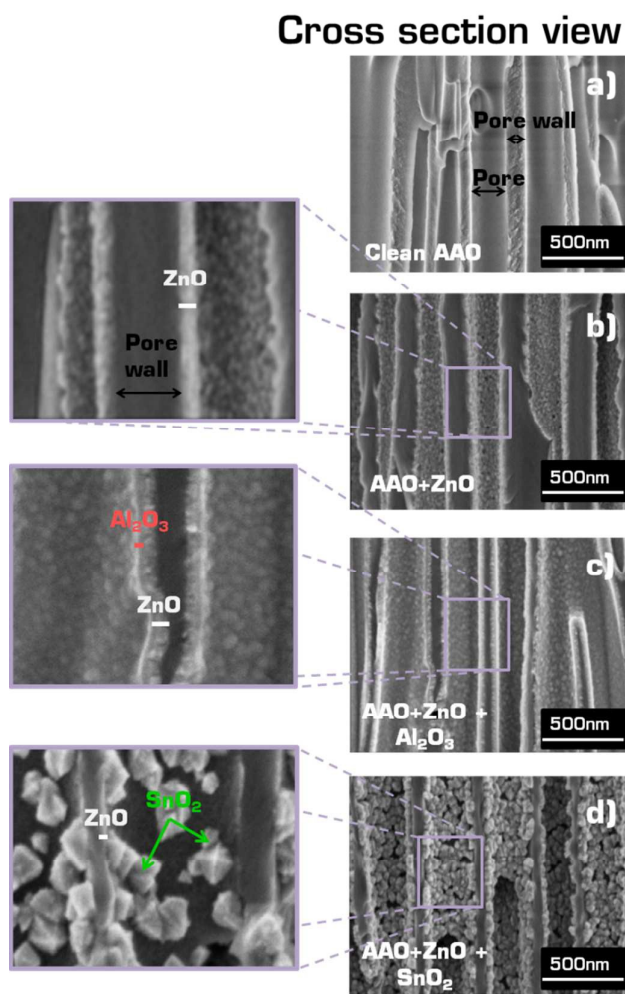


Figure 2 Cross-sectional and top view SEM pictures of anodic aluminium oxide on clean AAO (a), AAO/ ZnO (b), AAO/ $\text{ZnO}/\text{Al}_2\text{O}_3$ (c) and AAO/ ZnO/SnO_2 (d).

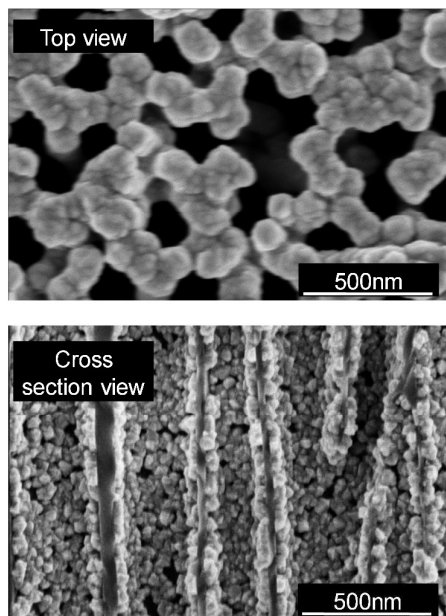


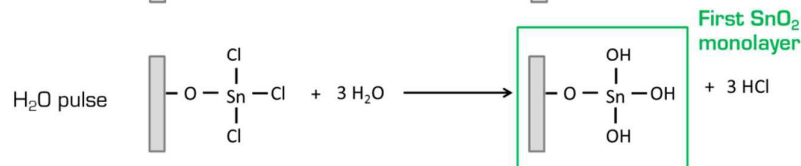
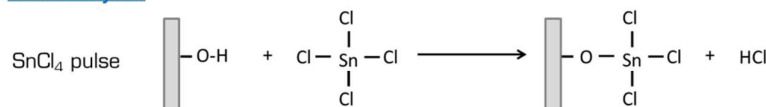
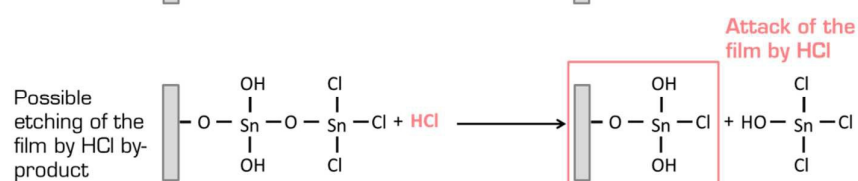
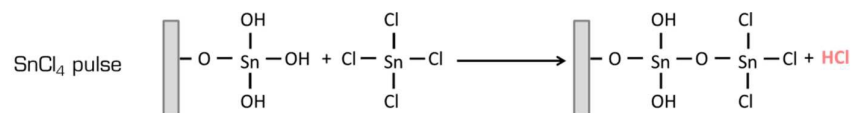
Figure 3: SEM pictures of SnO₂ deposited by ALD on the top of the AAO (top view) and inside the porous structure (cross section).

Table 1: XPS analysis of the relative elemental composition (expressed in at%) of the different elements present in the synthesised films.

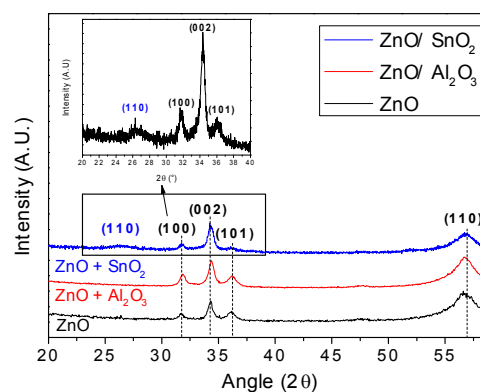
Samples	Elements (At% ±1%)				
	Zn	Al	Sn	O	C
ZnO in AAO	51	0	0	49	0
ZnO/Al ₂ O ₃ in AAO	1	35	0	60	4
ZnO/SnO ₂ in AAO	4	0	32	64	0

Structurally, ZnO thin films exhibit a pure hexagonal wurtzite crystalline phase (Figure 5). The XRD spectra exhibit the characteristic peaks corresponding to the (100), (002) and (101) crystallographic planes at 31.8 °, 34.25 ° and 36.15 °, respectively. The Al₂O₃ film on top of the ZnO thin film is an amorphous layer, as the XRD profile does not reveal any particular crystalline diffraction pattern corresponding to the former. We further confirm the hexagonal wurtzite structure of the ZnO underlying the Al₂O₃ layer. The tetragonal morphology of the tin oxide crystallites observed in the SEM images in the AAO samples was confirmed from the XRD spectra. Because of the thickness of the film, only the (110) crystallographic plane of the tetragonal cassiterite phase of SnO₂ appears at 26.54 °, while the other peaks in the spectrum correspond to the underlying wurtzite ZnO.

The ZnO wurtzite structure usually exhibits two luminescence bands. One is a narrow band located in the near visible region at approximately 380 nm (3.2 eV); emission in this region is also referred to as near band edge (NBE) emission. It is excitonic in nature and gives information on the direct electronic band gap of the material. The second band is broad and is located in a longer wavelength region with a maximum typically centred in the green at approximately 530 nm (2.33 eV). This band has been referred to as the deep level emission (DLE) band^{32,33}. Although the exact deconvolution of this peak is still being discussed in the literature, it is commonly accepted that its presence is due to defects in the material (zinc vacancies, zinc interstitial, oxygen vacancies, antisite oxygen). Because the optical signal is more intense on flat silicon, optical characterisations have been carried out on flat silicon substrates as well as on porous AAO. A weak excitonic peak appears at 380 nm in the obtained photoluminescence spectrum (Figure 6 a and b) for the ZnO grown on flat silicon. Following growth of the ZnO/Al₂O₃ films, the NBE emission at 380 nm

1st ALD cycle:**2nd ALD cycle:**Figure 4: Schema of the SnO₂ ALD reaction with a SnCl₄ precursor, showing the etching effect of HCl released in the porous membrane during the process

shows a tremendous five-fold improvement in intensity for both the planar and porous cases. In contrast, a quenching of this peak occurs for the ZnO/SnO₂ material. The 560 nm band in our spectra corresponds to the double excitation wavelength of the instrument light source and is unrelated to our material. One can notice that for all of the samples, no band appears in the visible range of the emission spectrum, which indicates that the ZnO films are of high quality and have few defects.

Figure 5: XRD analysis of ZnO, ZnO/Al₂O₃ and ZnO/SnO₂.

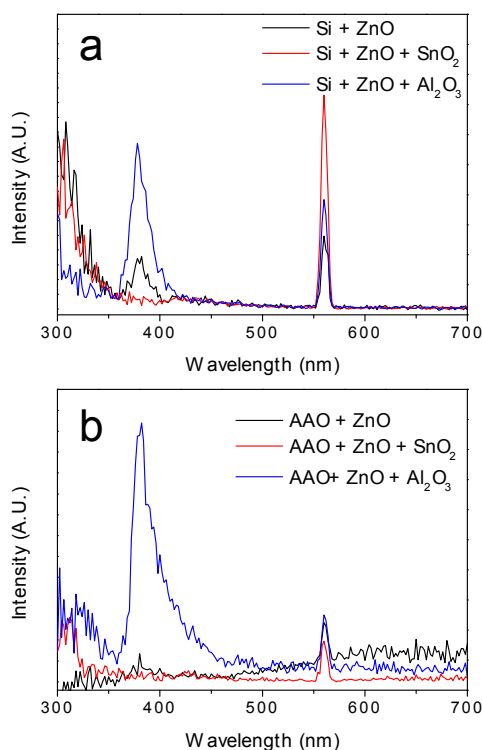


Figure 6: Photoluminescence spectra of ZnO, ZnO/Al₂O₃ and ZnO/SnO₂ for silicon substrate (a) or anodic aluminium oxide substrate (b).

The small intensity of the NBE exhibited by the ZnO film can be attributed to surface defects on the ZnO film (Figure 7). Adsorbed water molecules may have the effect of trapping free electrons generated in the conduction band to form charged oxygen molecules (O₂⁻, O⁻, O²⁻). As a result, an upward bend of the valence and conduction band is observed near the surface of the material¹¹, resulting in a widening of the depletion layer. This improves the separation of the photogenerated electron-holes carriers, enhancing their stabilisation. This effect prevents the radiative recombination of the electron-holes, facilitating a tunnelling recombination of the holes with deep levels of the charged oxygen³⁴. Electrons in the conduction band will recombine into those deep levels¹¹, which can lead to DLE emission or relaxation via a nonradiative pathway.

Considering that the thickness of the film is in the 20 nm range, the influence of the depletion layer may be crucial. The NBE peak originating from a thicker ZnO film (approximately 100 nm) was investigated and found to be more intense; therefore, the surface defects have less impact (Figure 8). During the Al₂O₃ ALD deposition, the oxygen defects present at the surface of ZnO participate in a reaction with the trimethylaluminium to form the first monolayer of Al₂O₃. Hence, those defects are no longer available to trap the photogenerated electrons in ZnO. Therefore, the alumina deposition acts as a dielectric barrier that screens the surface

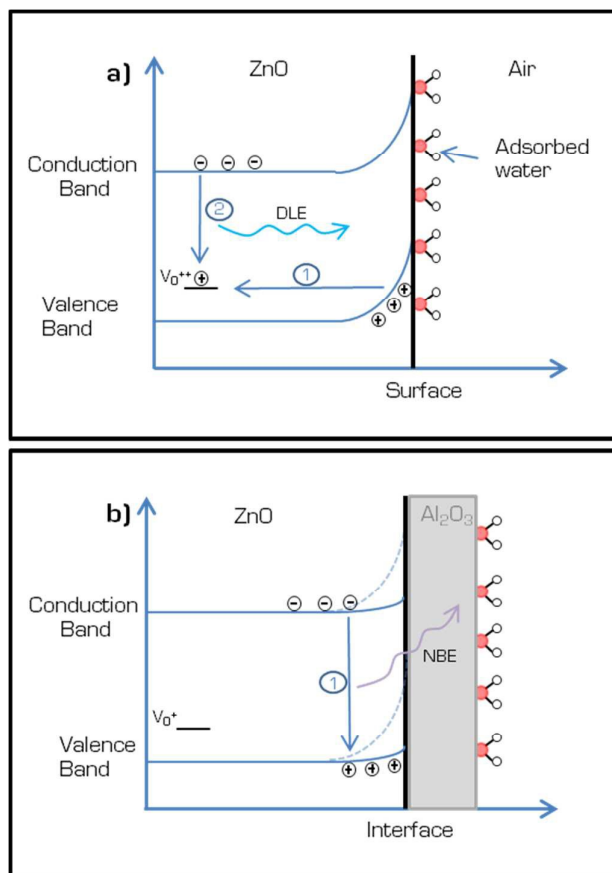


Figure 7: Schema of the surface of the ZnO and ZnO/Al₂O₃ films explaining the difference in the luminescent properties. Figure 6a) represents the surface of the ZnO film with adsorbed water molecules at the surface. Figure 6b) represents the ZnO/Al₂O₃ structure.

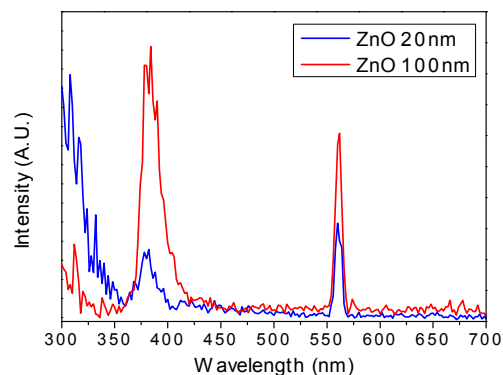


Figure 8: Photoluminescence spectra of ZnO films of different thickness.

defects, resulting in a lowering of the band bending in the ZnO structure. Consequently, the electron-hole wave function overlap at the surface of the material is stronger, which promotes the radiative recombination of excitons.

Kelvin probe force microscopy analyses were performed to verify the band bending theory. KPFM measures the contact potential difference (CPD) between a conductive tip and a material. When the tip approaches the surface, an electrical force is generated between the tip and the surface due to the difference in their Fermi energy levels. This force can be nullified if an external bias equal to the CPD is applied in the opposite direction. The amount of applied external bias is equal to the work function difference between the tip and the material analysed³⁵ (Figure 9).

The analysis of the ZnO layer led to an estimated CPD of -0.07 ± 0.02 V. Concerning ZnO/Al₂O₃, the CPD decreased to -0.357 ± 0.023 V (Table 2). Because Al₂O₃ is an ideal insulator, this decrease can be attributed to a downward band bending in ZnO, which is in good agreement with our previous hypothesis.

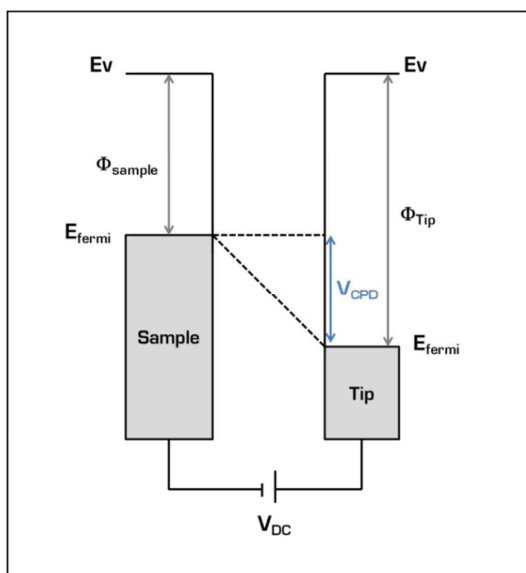


Figure 9: Schema of the KPFM principle for the analysis of a semi-conductor with a conductive tip.

Table 2: KPFM measurement of the CPD between the AFM tip and the ZnO and ZnO/Al₂O₃ films.

Material	ZnO	ZnO/Al ₂ O ₃
Contact Potential Difference (V)	-0.07 ± 0.02	-0.357 ± 0.023

In contrast to the enhancement of the NBE band after Al₂O₃ deposition, a quenching of the band is observed after SnO₂ deposition. This disappearance is attributed to the separation of the photogenerated electron-hole carriers due to the band alignment of ZnO and SnO₂ heterostructures. As depicted in Figure 10, in a ZnO/SnO₂ heterostructure band diagram, the energy of the valence band of the ZnO is higher than that of the SnO₂, and the energy of conduction band of the SnO₂ is lower than that of ZnO. As a result, the photogenerated electrons and holes in the ZnO/SnO₂ heterostructure tend to migrate, under the built-in electric field of the heterojunction, toward the conduction band of SnO₂, and toward the valence band of the ZnO, respectively. The separation of these electrons and holes lead to stable carriers with longer lifetime.

Thus, a decrease in the excitonic recombination rate can be observed, having for effect a weakened NBE emission band. In our case, this NBE band completely disappears. This charge carrier stability can be very useful for applications requiring performant charge separation, such as is the case with typical photocatalysis or photovoltaic devices³⁶.

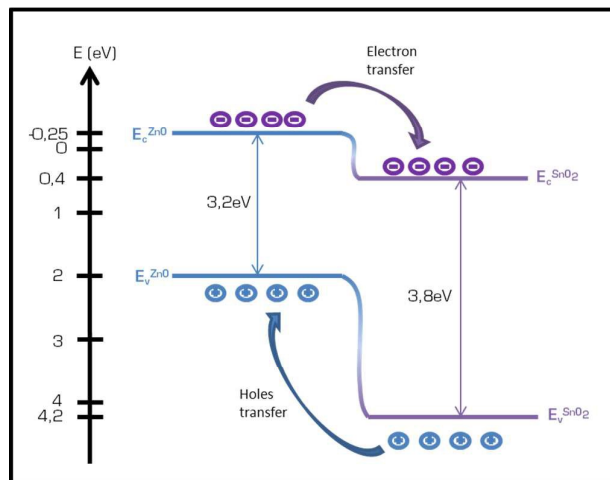


Figure 10: Schematic representation of the band diagram of the ZnO/SnO₂ heterostructure.

To precisely determine the band alignment in the ZnO/SnO₂ heterostructure, XPS analysis was performed using a procedure previously described in the literature^{37,38}. Indeed, the valence band offset (VBO or ΔE_v) as well as the conduction band offset (CBO or ΔE_c) in the heterostructure is estimated using

$$\Delta E_v = (E_{Zn2p} - E_{vZnO})_{ZnO \text{ bulk}} - (E_{Sn3d} - E_{vSnO_2})_{SnO_2 \text{ bulk}} - \Delta E_{CL} \quad [1]$$

where E_{Zn2p} corresponds to the binding energy of the Zn2p peak in bulk ZnO, E_{vZnO} to the valence band maximum of bulk ZnO, E_{Sn3d} to the binding energy of the Sn3d peak in bulk SnO₂ and E_{vSnO_2} to the valence band maximum in bulk SnO₂. The ΔE_{CL} term corresponds to

$$\Delta E_{CL} = (E_{Zn2p} - E_{Sn3d})_{\text{heterostructure}} \quad [2]$$

where E_{Zn2p} corresponds to the position of the Zn2p peak in the heterostructure of ZnO/SnO₂ and E_{Sn3d} corresponds to the position of the Sn3d peak in the heterostructure of ZnO/SnO₂. The conduction band offset (ΔE_c) can be calculated using

$$\Delta E_c = \Delta E_v + E_{gZnO} - E_{gSnO_2} \quad [3]$$

where ΔE_v is the valence band offset previously calculated, E_{gZnO} is the optical band gap of ZnO and E_{gSnO_2} is the optical band gap of SnO₂. Figure 11 highlights the high resolution XPS analysis of the Zn2p_{3/2} (a) and Sn3d_{5/2} (b) peaks as well as the VBM in ZnO bulk (c) and SnO₂ bulk (d) materials, respectively. The optical band gap of both materials (e and f) and the high

resolution XPS analysis of the Zn2p_{3/2} (g) and Sn3d_{5/2} (h) peaks in the ZnO/SnO₂ heterostructure is also presented.

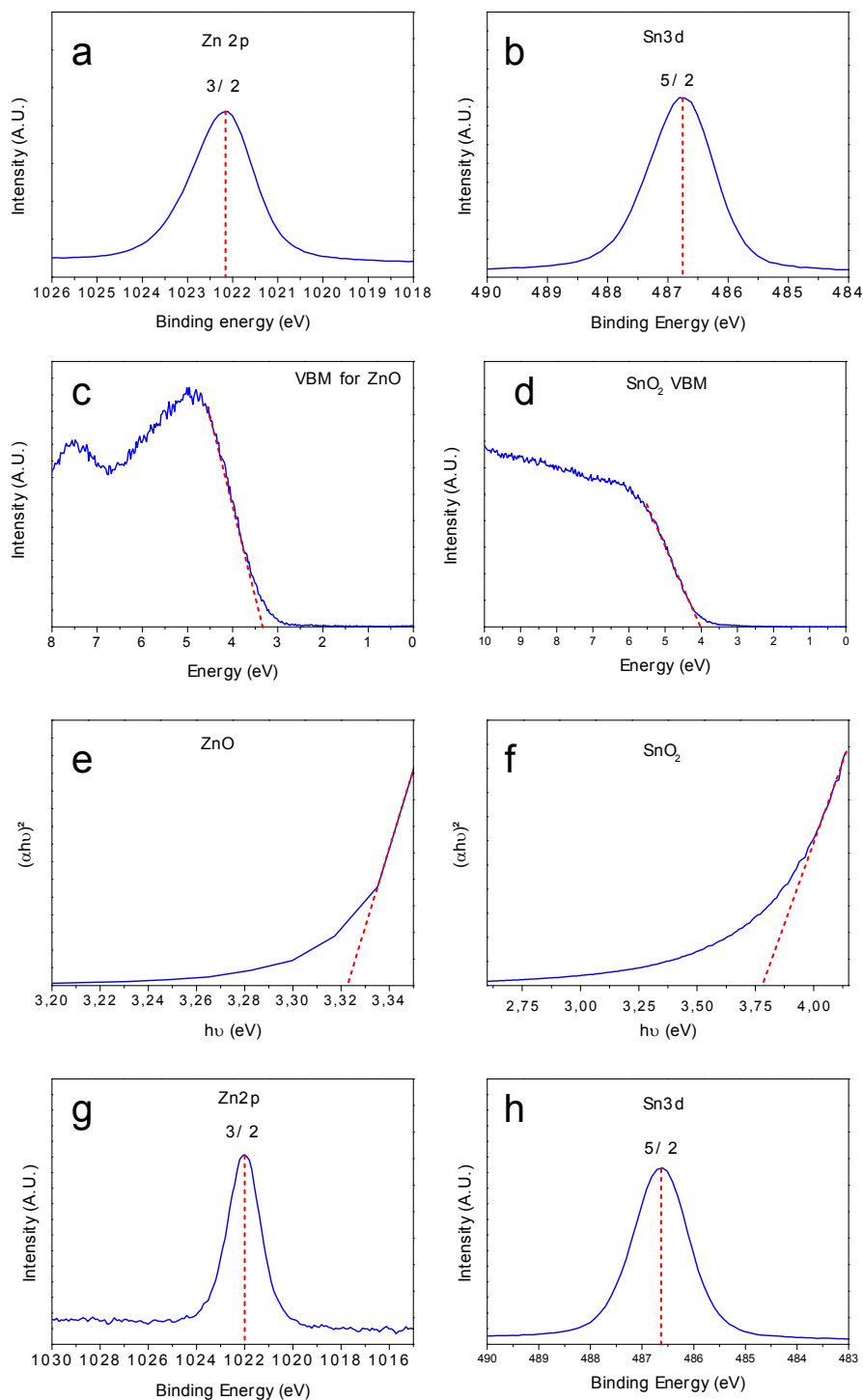


Figure 11: a) High resolution XPS analysis of the Zn2p peak in bulk ZnO. b) High resolution XPS analysis of the Sn3d peak in bulk SnO₂. c) Valence band maximum of bulk ZnO determined by high resolution UPS. d) Valence band maximum of bulk SnO₂ determined by high resolution UPS. e) Tauc plot of bulk ZnO. f) Tauc plot of bulk SnO₂. g) High resolution XPS analysis of the Zn2p peak in the heterostructure ZnO/SnO₂. h) High resolution XPS analysis of the Sn3d peak in the heterostructure ZnO/SnO₂.

Journal Name

ARTICLE

The exact binding energies along with the exact VBM position for each material are listed in Table 3. The optical band gap of bulk ZnO was measured to be approximately 3.3 eV (based on the Tauc plot), whereas it is measured to be approximately 3.7 eV for bulk SnO₂. These values are in good agreement with others contained in the literature^{39,40,41}.

Table 3: XPS binding energies and valence band maximum positions for bulk ZnO, bulk SnO₂ and the ZnO/SnO₂ heterostructure.

Material	State	Binding energy (eV)
Bulk ZnO	Zn2p _{3/2}	1022.12
	VBM _{ZnO}	3.31
Bulk SnO ₂	Sn3d _{5/2}	486.76
	VBM _{SnO2}	4.02
ZnO/SnO ₂	Zn2p _{3/2}	1022.01
	Sn3d _{5/2}	486.61

With the knowledge of the binding energies and VBMs for all of the materials, we calculated the VBO according to equation 1 and the CBO according to equation 3. The VBO and CBO were determined to be approximately 0.67 eV and approximately 0.24 eV, respectively. Similar results can be found in the literature⁴² concerning the band alignment in the ZnO/SnO₂ heterojunction, which confirms the presence of a type-II heterostructure observed between ZnO and SnO₂, as presented schematically in Figure 10.

The physico-chemical characterisation of ZnO, ZnO/Al₂O₃ and ZnO/SnO₂ films indicates an improvement in the optical emission properties of ZnO when covered with Al₂O₃, and the formation of a type II heterostructure with SnO₂. However, whether these bi-layer materials are highly attractive for optical or opto-chemical applications, their stability and biocompatibility as compared with ZnO remains to be determined.

Toxicity determination of the materials

Exposure of the Caco-2/TC7 cells to the AAO/ZnO samples after 24 hours in the absence of direct contact with the cells (exposure to the leachate of AAO/ZnO samples) resulted in a statistically significant decrease in cell viability by 30% compared with the untreated control ($P < 0.05$) (Figure 12). This highlights the toxic behaviour of our ZnO materials toward Caco-2/TC7 cells. It has been previously demonstrated that dissolution plays a critical role in ZnO NP-induced cytotoxicity in HaCaT cells, exhibiting a fast dissolution behaviour in an aqueous solution⁴³. Moreover, dissolution of the ZnO substrate affected the macrophage viability in the absence of direct contact between the substrate and the cells⁴⁴. In the case of ZnO/Al₂O₃ or ZnO/SnO₂, the metabolic activity of the

cells did not differ from that of the untreated control and from each other (Figure 12). The covering of ZnO with Al₂O₃ or SnO₂ seems to prevent the toxicity of the ZnO films observed previously. The relatively high standard deviation observed for ZnO/SnO₂ in particular indicates that material properties with respect to the leaching of ions may be different between batches of materials and that the processes may require some optimization in the future.

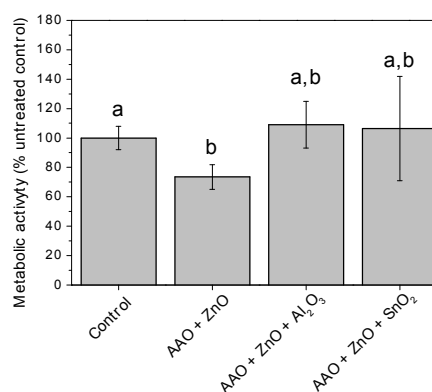


Figure 12: Effects of the ZnO, ZnO/Al₂O₃ and ZnO/SnO₂ nano-films in porous AAO on the metabolic activity of the Caco-2/TC7 cells in the absence of direct contact with the cells. The results are expressed relative to the untreated control.

Exposure of *V. fischeri* to the different materials in the absence of direct contact did not induce any harmful effects on the bacterial luminescence (Figure 13). The maximum concentration of Zn²⁺ ions released in water was below 0.3 mg.l⁻¹, which is below the reported half maximum effective concentration (EC50) of ZnO nanoparticles on *V. fischeri* of 2 mg.l⁻¹, and the EC20 of 1 mg.l⁻¹¹²⁵.

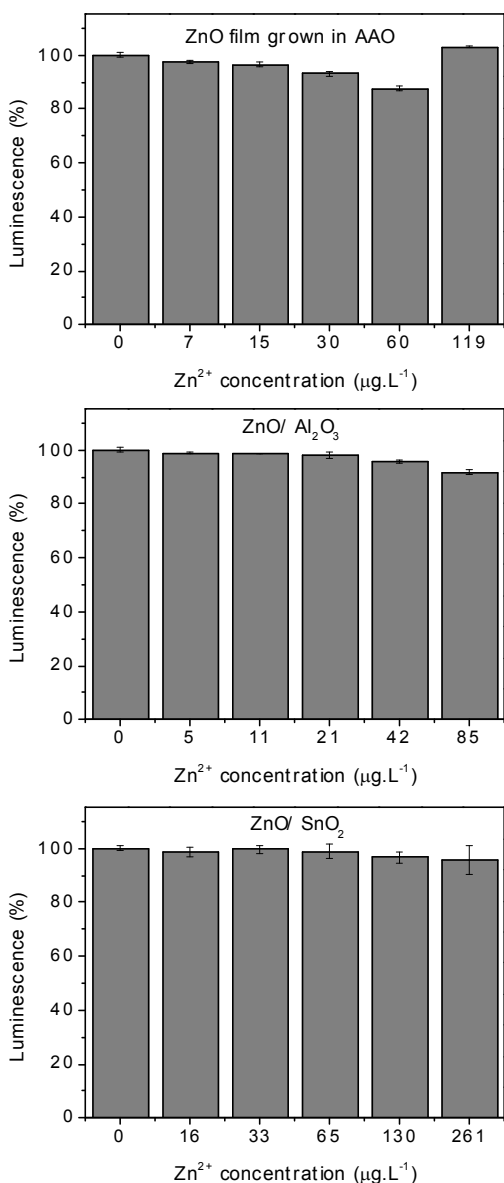


Figure 13: Effect of ZnO surfaces on *V. fischeri* luminescence. The results are expressed as the relative percentage of luminescence compared with the untreated control.

As there was no direct contact between the materials and the cells or bacteria, any toxicity observed on the cells must be due to ions leaching from the films in solution.

The dissolution of Zn²⁺ from the ZnO films in the cell culture medium was analysed by ICP-MS. The Zn²⁺ concentration after 24 h exposure was 36.6 mg.l⁻¹, which is more than 200 times higher than that measured in the control cell culture medium (Table 3). This clearly confirms the instability of ZnO films grown inside AAO in an aqueous solution. This dissolution behaviour can be a critical problem for the use of such materials in water treatment processes, or any other application in the liquid phase for which there is a possibility of uptake in humans. To overcome this problem, insoluble protective layers may be a solution for improving the stability of the ZnO material. However, the properties of ZnO that are of interest for technical applications should not be affected by the covering material. Al₂O₃ and SnO₂ grown on top of ZnO prevent cytotoxic effects. This is explained by the strong reduction in the leaching of free Zn ions after Al₂O₃ or SnO₂ deposition by a factor of 9 and 6, respectively (Table 4). Interestingly, Al₂O₃ and SnO₂ do not leach ions in aqueous solution as the concentrations of the respective ions were very low or even below the limit of detection. Thus, in addition to promoting the optical and opto-chemical properties of ZnO, Al₂O₃ and SnO₂ layers also lead to safer and more stable materials.

Table 4: ICP-MS measurement of the concentration of Zn soluble species in cell culture medium after 24 h exposure to the samples; nd = below limit of detection.

Material	Zn ²⁺ concentration (mg.l ⁻¹)	Al ³⁺ concentration (mg.l ⁻¹)	Sn ⁴⁺ concentration (mg.l ⁻¹)
ZnO	36.6	0.154	nd
ZnO/Al ₂ O ₃	4.2	0.074	nd
ZnO/SnO ₂	6.4	nd	nd
Cell culture medium (control)	0.17	0.08	nd

SEM surface analyses of the samples following the toxicological tests highlight the disappearance of the ZnO film (Figure 14) when it is not protected by another layer. These SEM images are in perfect agreement with the toxicological results performed on the cells and with the increase in zinc ions in the cell culture medium. In contrast, the Al₂O₃ and SnO₂ exposed surfaces remained unchanged.

Journal Name

ARTICLE

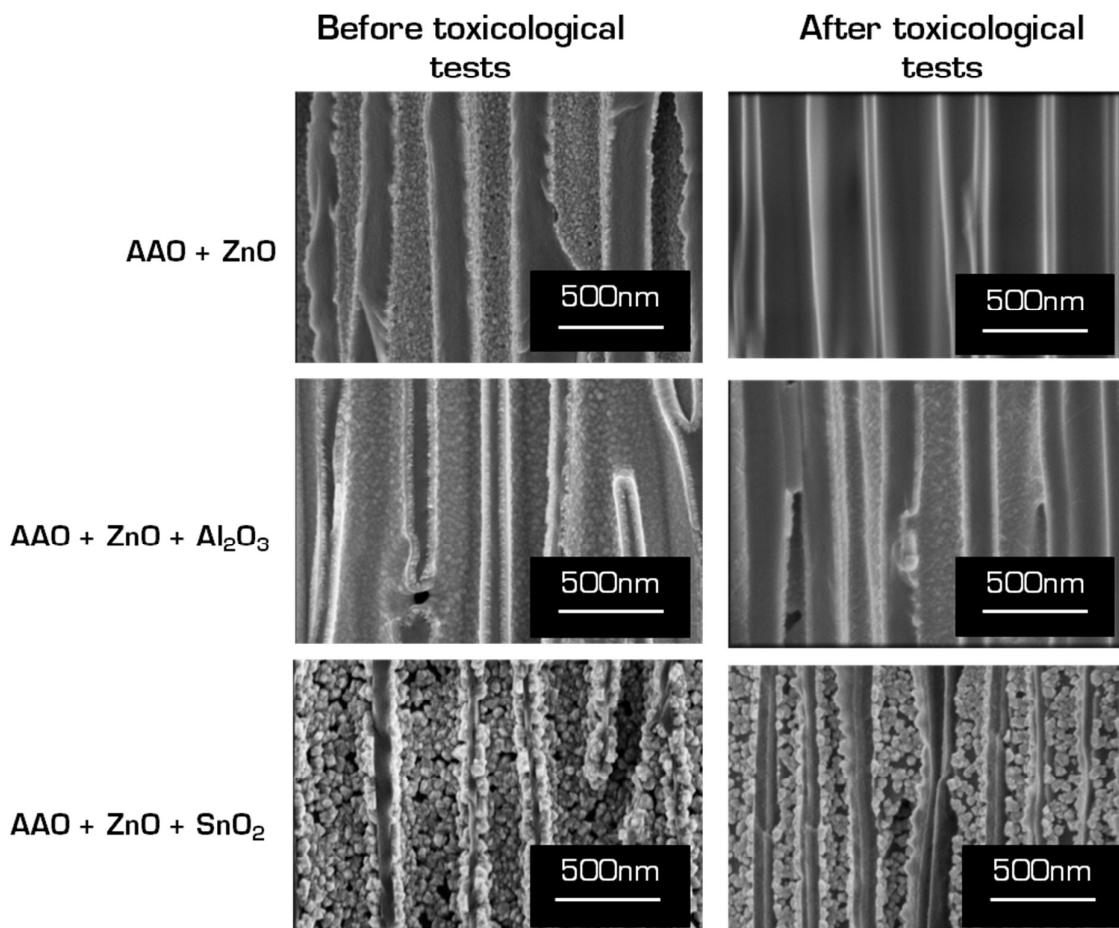


Figure 14: SEM cross-sectional view of ZnO, ZnO/Al₂O₃ and ZnO/SnO₂ before and after exposure to cell culture media for 24 h.

The XPS analysis of the surfaces further corroborates these results. In the case of deposition of only ZnO, the substrate used (porous alumina) is visible with 11 % of aluminium detected (Figure 15) following the toxicological test. This confirms the disappearance of the ZnO film, as no aluminium was detected prior to exposure to the cell culture medium. No zinc is observed for the ZnO/Al₂O₃ sample, indicating that the Al₂O₃ nano-film still homogeneously covers the entire surface of the ZnO. The analysis of the SnO₂ layer shows 7 % of Zn. Although this value is slightly higher compared with the analysis performed prior to the tests (4 %), it is still in the same range and does not indicate a critical loss of the material.

Instead, this result does confirm that the ZnO nano-film remains observable inside the porous structure. Interestingly, the ZnO/Al₂O₃ sample maintains its strong optical properties after exposure to cell culture medium (Figure 16). Although the excitonic luminescence intensity of the sample is reduced, it is still very strong compared with the unprotected ZnO sample. This highlights the ideal double role of the protecting layer of Al₂O₃ in both improving the optical properties of and protecting the ZnO layer.

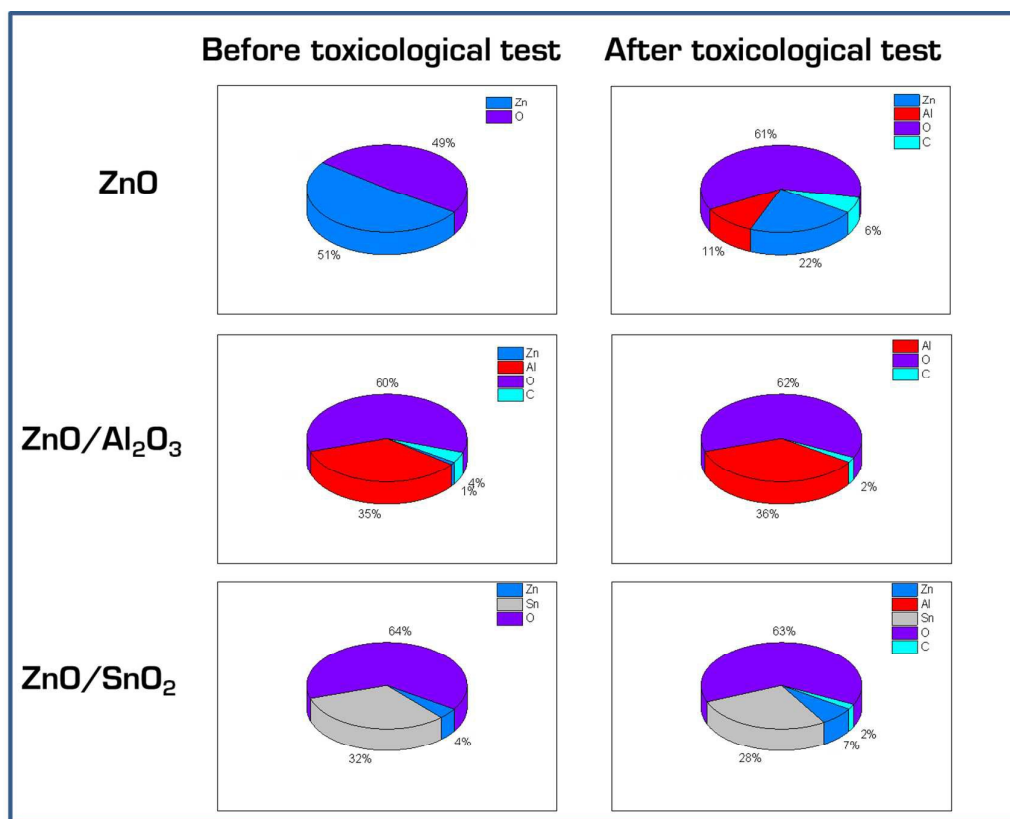


Figure 15: XPS analysis showing the stoichiometric composition of the ZnO, ZnO/Al₂O₃ and ZnO/SnO₂ layers after 24 h exposure to cell culture medium.

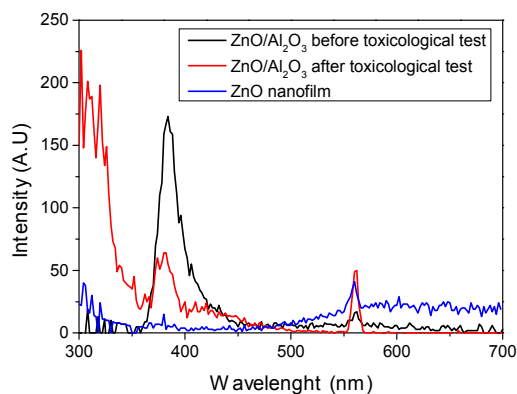


Figure 16: Photoluminescence spectra of ZnO/Al₂O₃ before and after the toxicological test.

Conclusions

The synthesis of ZnO, a ZnO/Al₂O₃ double layer, and a ZnO/SnO₂ heterostructure inside 3D materials such as AAO was carried out using a gas phase atomic layer deposition. With this deposition method, homogeneous and conformal ZnO and Al₂O₃ layers were deposited inside complex 3D porous AAO. Regarding the growth of SnO₂ materials in porous AAO, we have, to the best of our knowledge, demonstrated for the first time that tetragonal structures were obtained instead of a conformal film due to an acidic chemical attack of SnO₂ by HCl released from the precursor during the growth process. We note that a ZnO/Al₂O₃ heterostructure can promote the excitonic recombination of electrons and holes photogenerated in ZnO, leading to a significant increase in the NBE peak. In contrast, a ZnO/SnO₂ heterostructure promotes

the separation of the electrons and holes, which leads to a more stable photogenerated carriers, thus preventing their excitonic recombination. In addition, we demonstrated that these ZnO/Al₂O₃ and ZnO/SnO₂ multilayers helps improving the stability of the ZnO in aqueous environment, acting as protective layers. The result is an improved biocompatibility of such materials towards Caco-2 cells and *Vibrio fischeri* bacteria. The stability of ZnO/Al₂O₃ and ZnO/SnO₂ multilayers is witnessed with a low concentration of Zn²⁺ released in the aqueous medium compared to pure ZnO thin-films. We have evidenced the tailoring of the excitonic luminescence properties of ZnO/Al₂O₃ and ZnO/SnO₂ heterostructures and their biocompatibility. Combinatorial benefits of optical and biocompatibility properties are evidenced when devices based on ZnO heterostructures are engineered for their safe use in aqueous environments.

Acknowledgements

The authors would like to thank the “Fond National de la Recherche Luxembourgeoise” for the financial support of the Naneauil and Visicat projects (project number C10/SR/799 842 and INTER/NSF/MAT/11/01). The authors would also like to thank J. Didierjean for his contribution to the XPS analysis, J. Ziebel and C. Guignard for the ICP-MS measurements and S. Contal and A. Jehanno for the MTS analysis.

References

- 1 C. Klingshirn, *Phys. Status Solidi Basic Res.*, 2007, **244**, 3027–3073.
- 2 B.-Y. Oh, J.-H. Kim, J.-W. Han, D.-S. Seo, H. S. Jang, H.-J. Choi, S.-H. Baek, J. H. Kim, G.-S. Heo, T.-W. Kim and K.-Y. Kim, *Curr. Appl. Phys.*, 2012, **12**, 273–279.
- 3 S. S. Shinde, P. S. Shinde, C. H. Bhosale and K. Y. Rajpure, *J. Photochem. Photobiol. B Biol.*, 2011, **104**, 425–433.
- 4 M. Law, L. E. Greene, J. C. Johnson, R. Saykally and P. Yang, *Nat. Mater.*, 2005, **4**, 455–459.
- 5 Y. Jouane, S. Colis, G. Schmerber, P. Kern, a. Dinia, T. Heiser and Y. -a. Chapuis, *J. Mater. Chem.*, 2011, **21**, 1953.
- 6 H. Zhou, H. Alves, D. M. Hofmann, W. Kriegseis, B. K. Meyer, G. Kaczmarczyk and a. Hoffmann, *Appl. Phys. Lett.*, 2002, **80**, 210–212.
- 7 C.-J. Yang, S.-M. Wang, S.-W. Liang, Y.-H. Chang, C. Chen and J.-M. Shieh, *Appl. Phys. Lett.*, 2007, **90**, 033104.
- 8 A. B. F. Martinson, A. B. F. Martinson, M. J. Pellin, M. J. Pellin, J. T. Hupp and J. T. Hupp, *Society*, 2009, 4015–4021.

- 9 N. Kumar, G. D. Varma, R. Nath and a. K. Srivastava, *Appl. Phys. A*, 2011, **104**, 1169–1174.
- 10 W.-C. Sun, Y.-C. Yeh, C.-T. Ko, H. He and M.-J. Chen, *Nanoscale Res. Lett.*, 2011, **6**, 556.
- 11 J.-P. Richters, T. Voss, D. S. Kim, R. Scholz and M. Zacharias, *Nanotechnology*, 2008, **19**, 305202.
- 12 Y. J. Chiang and C. C. Lin, *Powder Technol.*, 2013, **246**, 137–143.
- 13 D. Sahu, G. M. Kannan, R. Vijayaraghavan, T. Anand and F. Khanum, *ISRN Toxicol*, 2013, **2013**, 316075.
- 14 M. J. Osmond-mcleod, Y. Oytam, R. I. W. Osmond, F. Sobhanmanesh and M. J. Mccall, *J. Nanomed. Nanotechnol*, 2014, **5**, 232.
- 15 I. De Angelis, F. Barone, A. Zijno, L. Bizzarri, M. T. Russo, R. Pozzi, F. Franchini, G. Giudetti, C. Uboldi, J. Ponti, F. Rossi and B. De Berardis, *Nanotoxicology*, 2012, **7**, 1–40.
- 16 S. Pokhrel, T. Xia, M. Kovochich, M. Liong, M. Schowalter, a. Rosenauer, B. Gilbert, J. I. Zink, a. E. Nel and L. Mädler, *Chemie Ing. Tech.*, 2009, **81**, 1167–1167.
- 17 C. Hanley, J. Layne, A. Punnoose, K. M. Reddy, I. Coombs, A. Coombs, K. Feris and D. Wingett, *Nanotechnology*, 2008, **19**, 295103.
- 18 M. Ahamed, M. J. Akhtar, M. Raja, I. Ahmad, M. K. J. Siddiqui, M. S. AlSalhi and S. a. Alrokayan, *Nanomedicine Nanotechnology, Biol. Med.*, 2011, **7**, 904–913.
- 19 H. C. Poynton, J. M. Lazorchak, C. a. Impellitteri, M. E. Smith, K. Rogers, M. Patra, K. a. Hammer, H. J. Allen and C. D. Vulpe, *Environ. Sci. Technol.*, 2011, **45**, 762–768.
- 20 M. Sarr, N. Bahlawane, D. Arl, M. Dossot, E. Mcrae and D. Lenoble, *J. Phys. Chem. B*, 2014, **118**, 23385–23392.
- 21 I. M. Sadiq, S. Pakrashi, N. Chandrasekaran and A. Mukherjee, *J. Nanoparticle Res.*, 2011, **13**, 3287–3299.
- 22 H. Wang, R. L. Wick and B. Xing, *Environ. Pollut.*, 2009, **157**, 1171–1177.
- 23 A. Basile, A. Cassano, *Woodhead P., Elsevier*, 2015.
- 24 I. Velzeboer, a J. Hendriks, A. M. J. Ragas and D. Van de Meent, *Environ. Toxicol. Chem.*, 2008, **27**, 1942–1947.
- 25 M. Heinlaan, A. Ivask, I. Blinova, H. C. Dubourguier and A. Kahru, *Chemosphere*, 2008, **71**, 1308–1316.

- 26 M. Macova, B. I. Escher, J. Reungoat, S. Carswell, K. L. Chue, J. Keller and J. F. Mueller, *Water Res.*, 2010, **44**, 477–492.
- 27 R. L. Puurunen, *Chem. Vap. Depos.*, 2005, **11**, 79–90.
- 28 J. Shi, C. Sun, M. B. Starr and X. Wang, *Nano Lett.*, 2011, **11**, 624–631.
- 29 X. Wang and J. Shi, *J. Mater. Res.*, 2013, **28**, 270–279.
- 30 J. Heo, A. S. Hock and R. G. Gordon, *Chem. Mater.*, 2010, **22**, 4964–4973.
- 31 D. Nazarov, *Rev. Adv Mater. Sci.*, 2015, **40**, 262–275.
- 32 M. Willander, O. Nur, J. R. Sadaf, M. I. Qadir, S. Zaman, A. Zainelabdin, N. Bano and I. Hussain, *Materials (Basel)*, 2010, **3**, 2643–2667.
- 33 V. Rogé, N. Bahlawane, G. Lamblin, I. Fechete, F. Garin, A. Dinia and D. Lenoble, *J. Mater. Chem. A*, 2015, **3**, 11453–11461.
- 34 C. Y. Chen, C. a Lin, M. J. Chen, G. R. Lin and J. H. He, *Nanotechnology*, 2009, **20**, 185605.
- 35 W. Melitz, J. Shen, A. C. Kummel and S. Lee, *Surf. Sci. Rep.*, 2011, **66**, 1–27.
- 36 M. Basu, N. Garg and A. K. Ganguli, *J. Mater. Chem. A*, 2014, **2**, 7517.
- 37 S. C. Su, H. Y. Zhang, L. Z. Zhao, M. He and C. C. Ling, *J. Phys. D: Appl. Phys.*, 2014, **47**, 215102.
- 38 R. Schlaf, O. Lang, C. Pettenkofer and W. Jaegermann, *J. Appl. Phys.*, 1999, **85**, 2732–2753.
- 39 V. B. Kamble and A. M. Umarji, *AIP Adv.*, 2013, **3**, 0–5.
- 40 P. Chetri and A. Choudhury, *Phys. E Low-Dimensional Syst. Nanostructures*, 2013, **47**, 257–263.
- 41 J. Wang, Z. Wang, B. Huang, Y. Ma, Y. Liu, X. Qin, X. Zhang and Y. Dai, *ACS Appl. Mater. Interfaces*, 2012, **4**, 4024–30.
- 42 T. Uddin, Y. Nicolas, T. Toupance, L. Servant, M. M. Mu, H. Kleebe, J. Ziegler and W. Jaegermann, *Inorg. Chem.*, 2012, **51**, 7764–7773.
- 43 P. L. Lee, B. C. Chen, G. Gollavelli, S. Y. Shen, Y. S. Yin, S. L. Lei, C. L. Jhang, W. R. Lee and Y. C. Ling, *J. Hazard. Mater.*, 2014, **277**, 3–12.

